

## Cell merging and the jet/downwelling ratio in Langmuir circulation

by Ming Li<sup>1</sup> and Chris Garrett<sup>1</sup>

### ABSTRACT

The Craik-Leibovich equations for Langmuir circulation have been integrated numerically to investigate the cell merging process as well as the strength and structure of the cells.

We find that pairs of counterrotating vortices cancel each other, leading to a growth in scale of the dominant vortices. However, when there is no external forcing, vortices of opposite sign do not merge irrespective of the vortex size and circulation strength. The merging of Langmuir cells, or rather the cancellation of counterrotating vortices, is thus different from the amalgamation of like-signed vortices in two-dimensional turbulence. The forcing due to the Stokes drift plays an important role in the cell-merging process.

As the Langmuir number  $La$  decreases, the maximum downwelling velocity increases while the pitch (the ratio of surface downwind jet strength to the maximum downwelling velocity) decreases. When  $La$  is about 0.01, as for an eddy viscosity in the range of values commonly used for the ocean surface layer, the model predicts a maximum downwelling velocity of 0.006 to  $0.01U_w$  (the wind speed), comparable with the observed magnitude. However, the surface downwind jet is significantly weaker than the observed strength.

At small  $La$  a simple scale analysis, which couples a surface boundary layer with a narrow downwelling region, suggests that the thickness of these regions should vary as  $La^{1/2}$ , the downwelling velocity as  $La^{-1/3}$  and the pitch as  $La^{1/6}$ . These predictions are supported by numerical results.

### 1. Introduction

Langmuir circulation consists of a pattern of parallel vortices oriented downwind, of alternating sense of circulation or vorticity, and with maximum downwind surface current at the surface convergences. It may promote vertical mixing in the upper ocean (Langmuir, 1938; Pollard, 1977; Leibovich, 1983) and contribute to horizontal dispersion (Faller and Auer, 1988; Thorpe, 1992a,b), but its precise effects are still poorly understood (see Thorpe 1992a, b).

Much effort has been devoted to explaining the generation of the Langmuir cells. In a series of papers Craik and Leibovich developed a model that now bears their name, the CL2 model (e.g. Craik and Leibovich, 1976; Craik, 1977; Leibovich, 1977b;

1. Centre for Earth and Ocean Research, University of Victoria, Victoria, British Columbia, Canada V8W 2Y2.

Leibovich and Paolucci, 1980, 1981). They argued that Langmuir cells are an instability associated with the interaction between the Stokes drift current and the wind-driven shear current. The CL2 instability mechanism consists of two indispensable parts: the generation of streamwise vorticity and the reinforcement of the downwind jet.

Leibovich (1977b, 1983) used the concept of vortex force to explain how a spanwise anomaly of downwind current creates streamwise vorticity. Suppose an infinitesimal spanwise irregularity  $u'(y, z, t)$  is present in an otherwise horizontally uniform current  $U(z, t)$ . This produces vertical vorticity  $\Omega_z = -\partial u' / \partial y$  and a horizontal vortex-force component  $-u_s \Omega_z \mathbf{j}$  ( $u_s$  is the Stokes drift) that is directed toward the plane of maximum  $u'$ . This causes an acceleration toward these planes, where, by continuity, the fluid must sink. The kinematic interpretation is that the vertical gradient of the Stokes drift tilts the vertical vortex line associated with the spanwise variation of the downwind current, thereby creating streamwise vorticity.

The instability also requires a mechanism to reinforce the downwind jet. Leibovich and Paolucci (1980) argued that a water particle brought to the surface away from the surface convergence is accelerated by the wind stress as it is swept toward the convergence line (or the downwelling site), driving the jet there. This argument is physically plausible but ignores the friction exerted by neighboring water particles and cannot be applied at the center of the convergence zones where the cross-jet flow is zero. We shall demonstrate that on this line the water particle is accelerated by the wind because the viscous friction is greatly reduced. To summarize, the downwind jet at the water surface is reinforced because the water particle is accelerated by the wind stress as it is swept toward the convergence line and feels less viscous friction at the downwelling site.

The merging of Langmuir cells has been observed frequently (Langmuir, 1938; see Leibovich (1983) for a review), and plays an important role in the horizontal dispersion of floating material or bubbles (Thorpe, 1992b). In recent experiments Weller and Price (1988) found that computer cards used as surface drifters are continuously drawn into longer lines separated by greater distances. Using sidescan sonar, Thorpe (1992b) observed that bubble bands with a relatively small separation have an apparent motion toward larger-scale, more persistent neighboring bands.

It has been speculated (Faller and Auer, 1988) that the evolution of large Langmuir cells from small ones is analogous to the "inverse energy cascade" in two-dimensional turbulence. We find that unforced counterrotating vortices do not merge irrespective of the circulation strength and vortex size. Langmuir cells do grow in scale, however, when the forcing due to the Stokes drift is included. Thus the growth in scale of Langmuir cells through cancellation of opposite-signed vortices is different from the amalgamation of like-signed vortices in two-dimensional turbulence.

The CL2 model is self-consistent and is able to reproduce qualitative features observed in Langmuir circulation, but a detailed quantitative comparison between the model and observations appears to be lacking. In this paper two key quantities will be used to test the model prediction. One is the maximum downwelling velocity and the other is the pitch representing the ratio of the downwind jet strength to the maximum downwelling velocity. Weller and Price (1988) observed a downwelling velocity up to  $0.3 \text{ m s}^{-1}$  with comparable magnitude for the downwind velocity. We shall show that, by adjusting the eddy viscosity, the CL2 model can account for the downwelling velocity, but the downwind jet predicted by the model is weaker than observed.

## 2. Nondimensionalization

Leibovich (1977a) averaged the Navier-Stokes equations on a time scale much longer than the surface wave periods and the turbulence time scale, and obtained the governing equations for Langmuir circulation. Ignoring density stratification, these are

$$\begin{aligned} \frac{\partial \bar{u}}{\partial \bar{t}} + \bar{v} \frac{\partial \bar{u}}{\partial \bar{y}} + \bar{w} \frac{\partial \bar{u}}{\partial \bar{z}} &= \nu_T \nabla^2 \bar{u}, \\ \frac{\partial \tilde{\Omega}}{\partial \bar{t}} + \bar{v} \frac{\partial \tilde{\Omega}}{\partial \bar{y}} + \bar{w} \frac{\partial \tilde{\Omega}}{\partial \bar{z}} &= \nu_T \nabla^2 \tilde{\Omega} - \frac{d\bar{u}_s}{d\bar{z}} \frac{\partial \bar{u}}{\partial \bar{y}}, \\ \tilde{\Omega} &= \nabla^2 \tilde{\psi}, \\ \bar{v} &= -\tilde{\psi}_z, \quad \bar{w} = \tilde{\psi}_y, \end{aligned}$$

in which  $\bar{u}$ ,  $\bar{v}$ ,  $\bar{w}$  are the downwind, spanwise and vertical velocity components, respectively,  $\tilde{\Omega}$  is the streamwise vorticity and  $\bar{u}_s$  is the Stokes drift current. This set of equations can also be derived (Leibovich, 1980) by using the generalized Lagrangian mean description of Andrews and McIntyre (1978).

Four input parameters for Langmuir circulation are the friction velocity  $u_*$  representing the wind stress applied at the water surface, the surface value  $2S_0$  and  $e$ -folding depth  $1/(2\beta)$  of the Stokes drift current, and the eddy viscosity  $\nu_T$ . In Leibovich's original formulation, wave height and wave length of the dominant wave were chosen as the input parameters, but ocean surface waves have a broad spectrum, with no discernible peaks in fully developed seas. It would be difficult to select the dominant wave from the wave spectrum. According to Craik-Leibovich theory, however, what really matters in Langmuir circulation is the Stokes drift. Kenyon (1969) and Huang (1971) calculated the Stokes drift for random surface waves by using the directional wave spectrum and found that the Stokes drift current may be approximated by an exponential profile. We thus replace the wave parameters with the surface value  $2S_0$  and  $e$ -folding depth  $1/(2\beta)$  of the Stokes drift in our parameterization.

Nondimensionalization leads to the Craik-Leibovich equations

$$\frac{\partial u}{\partial t} + v \frac{\partial u}{\partial y} + w \frac{\partial u}{\partial z} = La \nabla^2 u, \tag{1}$$

$$\frac{\partial \Omega}{\partial t} + v \frac{\partial \Omega}{\partial y} + w \frac{\partial \Omega}{\partial z} = La \nabla^2 \Omega - \frac{du_s}{dz} \frac{\partial u}{\partial y}, \tag{2}$$

$$v = -\frac{\partial \Psi}{\partial z}, \quad w = \frac{\partial \Psi}{\partial y}, \quad \Omega = \nabla^2 \Psi, \tag{3}$$

where the nondimensionalized Stokes drift has the form

$$u_s = 2e^{2z}$$

and the Langmuir number  $La$  is defined as

$$La = \left(\frac{\nu_T \beta}{u_*}\right)^{3/2} \left(\frac{S_0}{u_*}\right)^{-1/2} \tag{4}$$

The Langmuir number is thus inversely related to the Reynolds number and represents the ratio of viscous to inertial forces. It can be also interpreted as the ratio of the rate of diffusion of vorticity to the rate of production of streamwise vorticity by the vortex tilting accomplished by the Stokes drift.

The boundary conditions at the surface are

$$\Psi(y, 0, t) = \Psi_{zz}(y, 0, t) = 0, \tag{5}$$

$$u_z(y, 0, t) = 1. \tag{6}$$

Dimensional and nondimensionalized quantities are related through the following formulae:

$$\frac{\tilde{u}}{u_*} = \left(\frac{S_0}{u_*}\right)^{-1/3} La^{-2/3} u, \tag{7}$$

$$\left(\frac{\tilde{v}}{u_*}, \frac{\tilde{w}}{u_*}\right) = \left(\frac{S_0}{u_*}\right)^{1/3} La^{-1/3} (v, w), \tag{8}$$

$$\frac{\tilde{t}}{1/(u_* \beta)} = \left(\frac{S_0}{u_*}\right)^{-1/3} La^{1/3} t, \tag{9}$$

$$\frac{\tilde{\Omega}}{u_* \beta} = \left(\frac{S_0}{u_*}\right)^{1/3} La^{-1/3} \Omega. \tag{10}$$

It should be noted that there are two dimensionless parameters  $La$  and  $S_0/u_*$  in the model, but that  $S_0/u_*$  does not appear in the governing equations.

### 3. The friction velocity and Stokes drift

To compare model predictions with observations, we need estimates of the water friction velocity, the eddy viscosity and the Stokes drift. The wind stress  $\tau_w$  is related to the wind speed  $U_w$  (typically measured at 10 m above the sea surface) through an empirical formula

$$\tau_w = \rho_a C_D U_w^2 \quad (11)$$

where  $\rho_a$  is the air density and  $C_D$  is the drag coefficient determined from experimental observations. For wind speeds between 5 and 25 m s<sup>-1</sup>,  $C_D$  increases with wind speed from  $0.88 \times 10^{-3}$  to  $1.88 \times 10^{-3}$  (Smith, 1988).

The net transfer of momentum to the current in the mixed layer is the wind stress less the local growth of surface wave momentum and the divergence of the surface wave momentum flux. Using the JONSWAP wave observations (Hasselmann *et al.*, 1973), Richman and Garrett (1977) found that 97% of the wind stress  $\tau_w$  is transferred to the current; in fully developed seas, most of the momentum transfer is through wave breaking (e.g. Thorpe, 1992a).

Assuming thus that all the wind stress goes to drive the current, the water friction velocity is

$$\begin{aligned} u_* &= \left( \frac{\tau_w}{\rho_w} \right)^{1/2} = \left( \frac{\rho_a}{\rho_w} C_D \right)^{1/2} U_w \\ &= \left( \frac{1}{950} \text{ to } \frac{1}{650} \right) U_w. \end{aligned} \quad (12)$$

using typical values of  $C_D$ .

Huang (1971) derived a general formula for the Stokes drift for random surface gravity waves,

$$\tilde{\mathbf{u}}_s = \int_{\mathbf{k}} 2\sigma \mathbf{k} E(\mathbf{k}) e^{-2|\mathbf{k}|z} d\mathbf{k}, \quad (13)$$

where  $\sigma$  is the frequency,  $\mathbf{k}$  is the wavenumber vector and  $E(\mathbf{k})$  is the directional wave spectrum.

Using the empirical Pierson and Moskowitz spectrum

$$E(\sigma) = \alpha g^2 (2\pi)^{-4} \sigma^{-5} \exp \left[ -\frac{5}{4} \left( \frac{\sigma}{\sigma_m} \right)^{-4} \right] \quad (14)$$

for fully developed seas, we get

$$\tilde{u}_s(\tilde{z}) = 0.016 U_w \int_0^{f_c} \frac{1}{f^2} \exp [-0.7484f^{-4} + 2f^2 z^*] df \quad (15)$$

in which

$$f = \frac{U_w \sigma}{g} \quad \text{and} \quad z^* = \frac{g \bar{z}}{U_w^2} \quad (16)$$

with  $g$  being the gravitational acceleration. The cut-off frequency  $f_c$  is chosen so that the first three significant digits of the Stokes drift current velocity remain the same even if  $f_c$  is made higher.

The surface Stokes drift is

$$\tilde{u}_s(0) = 2S_0 = 0.016U_w, \quad (17)$$

in agreement with Kenyon (1969).

The effect of an angular spread in the wave spectrum would be to decrease the Stokes drift component in the principle direction of wave propagation. For example, for the symmetric spreading factor

$$S(\alpha) = \cos^m \alpha \quad \text{for} \quad |\alpha| \leq \pi/2,$$

the Stokes drift in the direction  $\alpha = 0$  is reduced by a factor 0.91 for  $m = 4$  and 0.85 for  $m = 2$ . Thus we have

$$\tilde{u}_s(0) = 2S_0 = (0.014 - 0.015)U_w. \quad (18)$$

Combining (12) and (18), we have

$$\frac{S_0}{u_*} = 4.6 \text{ to } 6.9. \quad (19)$$

The  $e$ -folding depth of the Stokes drift calculated from the Pierson and Moskowitz spectrum is found to be

$$\frac{1}{2\beta} = 0.12 \frac{U_w^2}{g}. \quad (20)$$

One can express the eddy viscosity in terms of the Langmuir number as

$$\begin{aligned} \frac{\nu_T}{u_* / \beta} &= \left( \frac{S_0}{u_*} \right)^{1/3} La^{2/3} \\ &\approx 0.077 \text{ to } 0.088 \quad \text{for} \quad La = 0.01, \\ &\approx 0.017 \text{ to } 0.019 \quad \text{for} \quad La = 0.001. \end{aligned}$$

With  $La = 0.01$  to  $0.001$ , the value of eddy viscosity compares favorably with the estimates given in Huang (1979).

#### 4. Spectral simulation

In spectral methods the solution is expanded as a series of the basis functions (or trial functions) (e.g. Canuto *et al.*, 1987). The test functions are chosen to ensure that

the differential equation is satisfied as closely as possible by the truncated series expansion. We shall adopt a Fourier Galerkin method in our model, in which both the trial functions and the test functions are chosen to be Fourier series.

The stress boundary condition (6) at the water surface can be made homogeneous by separating the  $x$ -component velocity into two parts, namely  $u = U(z, t) + u'(y, z, t)$  in which  $U(z, t)$  is the basic current, uniform in the spanwise direction, and  $u'(y, z, t)$  is the perturbation current. Two forms of  $U(z, t)$  are used in our model. One is the steady Couette flow, which satisfies a no-slip condition at the bottom boundary. In this case the wind stress applied at the surface is totally supported by the frictional resistance at the bottom boundary. Another choice is the developing similarity flow given by

$$U(z, t) = 2(Lat)^{1/2}f(\eta) \quad (21)$$

where

$$\eta = \frac{z}{2(Lat)^{1/2}},$$

$$f(\eta) = \pi^{-1/2}e^{-\eta^2} + \eta \operatorname{erfc}(-\eta).$$

In this case the bottom cannot support the total velocity shear. The velocity shear  $\partial U/\partial z$  for the two forms of  $U(z, t)$  is the same near the water surface, and this may be all that matters (see later).

Subtracting the equation for  $U(z, t)$  in (1), we get for the perturbation downwind current  $u'(y, z, t)$

$$\frac{\partial u'}{\partial t} + v \frac{\partial u'}{\partial y} + w \left( \frac{\partial u'}{\partial z} + \frac{dU}{dz} \right) = La \nabla^2 u'. \quad (22)$$

Following Leibovich *et al.* (1989), we shall consider a model in which the surface stress remains constant. Thus perturbations  $u'(y, z, t)$  are considered stress-free at both upper and lower boundaries. Written in mathematical terms, the boundary conditions at the top and bottom boundaries of the layers are

$$\psi = \frac{\partial^2 \psi}{\partial z^2} = \frac{\partial u'}{\partial z} = 0 \quad \text{at} \quad z = 0, -\beta d \quad (23)$$

where  $\beta d$  is the depth of the layer.

Periodic boundary conditions are imposed at the two lateral boundaries, i.e.

$$\psi(y + \beta L) = \psi(y), \quad u'(y + \beta L) = u'(y). \quad (24)$$

The horizontal extent  $\beta L$  of the cells is an unknown and cannot be determined from the model, as noted by Leibovich and Paolucci (1980) and Cox *et al.* (1992). In most

runs we choose a computational box with  $\beta L = 2\pi$  and  $\beta d = \pi$ , so that the Stokes drift which provides the forcing drops to less than 0.002 of its surface value at the bottom boundary, but we will later double both the horizontal and vertical scales of the computational domain to examine the sensitivity of the numerical results.

The solutions  $\psi$  and  $u'$  are expanded as Fourier series in both  $y$  and  $z$  directions and are chosen so that the imposed boundary conditions are satisfied. The spatial resolution is chosen such that the one-dimensional energy spectra show exponential decay at high wavenumbers. It is found that  $64 \times 64$  or  $128 \times 128$  Fourier modes provide adequate resolution for the  $La$  regime studied in this paper (generally speaking, high resolution is required at low  $La$ ).

An infinitesimal random disturbance is imposed for the vorticity distribution and the perturbation  $u'$  is set to zero at  $t = 0$ . To ascertain whether the solution is sensitive to the initial setup of the model and because we do not know precise initial data, we have tried other types of initial conditions. For example, two counterrotating vortices of finite strength are imposed for the vorticity distribution. In conjunction, a prescribed jet is imposed as the initial downwind current. We find that, for  $La$  in the range of 0.01 to 0.1, the same flow patterns are established after an early adjustment stage. During this adjustment stage, the prescribed vortices are being replaced by vortices which are solutions of the Craik-Leibovich equations. Thus it appears that the quasi-steady solutions of the CL2 model are insensitive to the initial setup.

## 5. The evolution of Langmuir cells

The spectral code is used to follow the time evolution of Langmuir cells. Cells of relatively small size appear first and grow in scale until a quasi-steady state is reached.

### *a. Merging process*

It has been suggested (e.g. Faller and Auer, 1988) that the merging of Langmuir cells is analogous to the inverse energy cascade in two-dimensional turbulence. We shall demonstrate, however, that unforced counterrotating vortices cannot merge in any case and that the growth in scale of Langmuir cells is due to forcing by the Stokes drift.

*i. Unforced.* When no external forcing is present in a weakly dissipative vortex system, vortices are driven around by each other. In agreement with Melander *et al.* (1988), we find that two prescribed corotating vortices merge into a bigger vortex if their original locations are sufficiently close together.

On the other hand, a pair of counterrotating vortices sitting at an upwelling site pair up with their respective image vortices and move apart, even when they are

unequal in size or strength. When two counterrotating vortices of the same size and vortex strength are located at a downwelling site, they sink vertically as a dipole. If the members of this vortex pair differ in size or strength, the weak vortex swings around the strong vortex as they both translate. Irrespective of circulation strength and vortex size, however, none of the vortices of opposite sign have merged in our numerical simulations.

*ii. Forced.* In contrast with the unforced situation, counterrotating Langmuir cells grow in scale when the forcing due to the Stokes drift is considered as in the CL2 model. To illustrate the cell-merging process, we show snapshots of vorticity and downwind current contours taken sequentially in time (Fig. 1). In this example  $La = 0.02$  and the basic current  $U(z, t)$  is the developing similarity flow. We start with an infinitesimal random distribution of vorticity and assume that at  $t = 0$  the wind is switched on to drive the current.

Rotating cells of alternating sign are generated shortly after the inception, with different cell sizes coexisting. The cells are rather weak initially and the downwind current at  $t = 10$  is barely disturbed from  $U(z, t)$ . However, both the circulation of the cells and the downwind current anomaly increase with time. In the contour plots at  $t = 20$ , three pairs of counterrotating vortices are observed and are associated with three maxima of the total downwind current.

At  $t = 30$ , we see that the two vortices located close to the left side of the box are being squeezed by their neighboring vortices. The third one on the left and last one on the right expand horizontally. In the contours of the total downwind current, two maxima approach each other. Since periodic conditions are imposed at the lateral boundaries, it is easier to visualize the flow pattern if we envisage two boxes of the same flow field to the left and right of the box shown. In the next snapshot, two cells of opposite sign have cancelled and only four cells are left. Accordingly, only two maxima of the downwind current remain. This vortex-cancellation process repeats itself until the cells reach a quasi-steady state. At  $t = 40$ , two cells situated in the neighborhood of the two lateral boundaries are being pushed by the middle two. Two maxima of the downwind jet are being pulled together. The cancellation of these two vortices is completed at  $t = 60$ . We are then left with two counterrotating cells and one maximum of the downwind current. Thereafter the flow structure within the two cells shows no significant change, although the cells drift slightly to the right.

By comparing the results in the unforced and forced situations, we can conclude that the merging of Langmuir cells, or rather the cancellation of counterrotating vortices, is different from vortex merging in two-dimensional turbulence. There the dominant mechanism for the inverse energy cascade is through the merging of like-signed vortices. The two key assumptions used in two-dimensional turbulence, namely the conservation of energy and enstrophy (or vorticity), cannot be made in Langmuir circulation. Moreover, in the CL2 model, the forcing term due to the

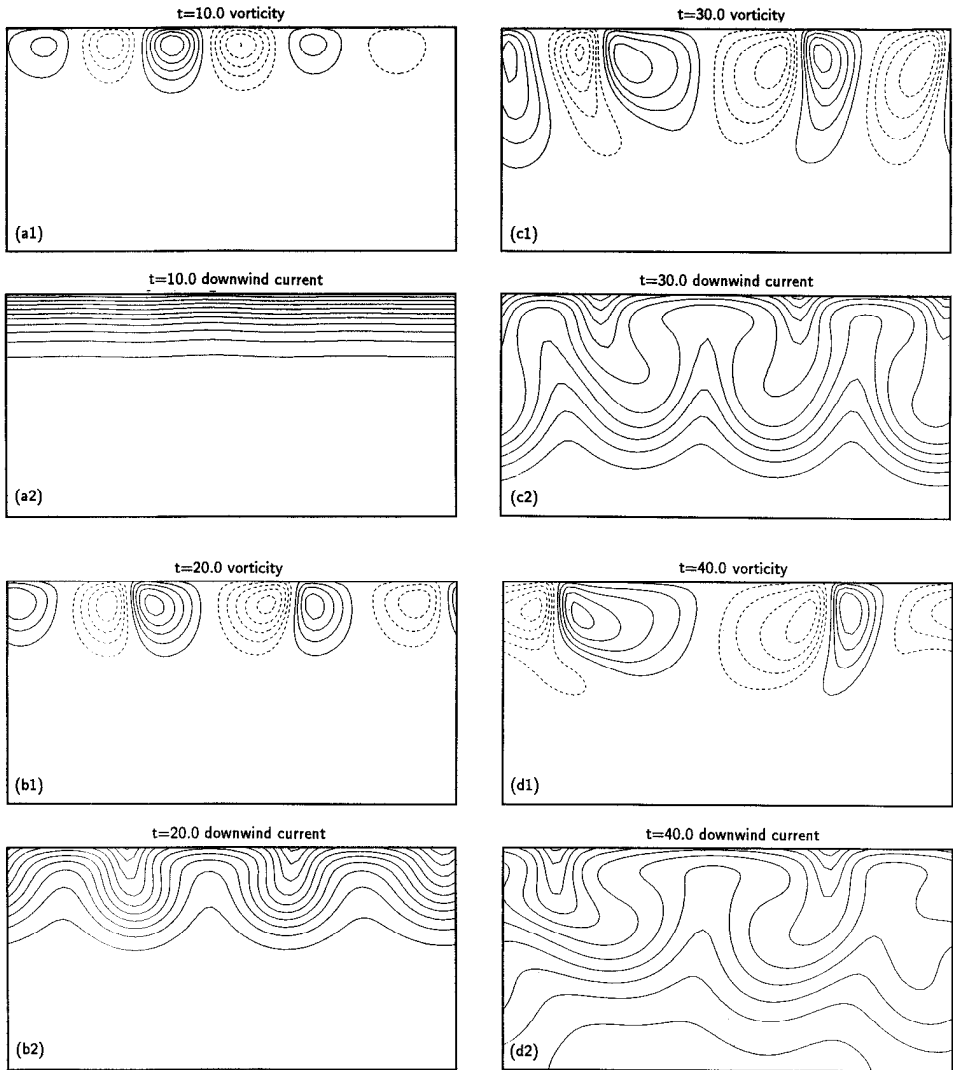


Figure 1. Snapshots of vorticity and downwind current contours at different dimensionless times.  $La = 0.02$  and the box size is defined by  $\beta L = 2\pi$  and  $\beta d = \pi$ . The basic current  $U(z, t)$  is the developing current.

Stokes drift is as important as the advection term in the vorticity equation (2). Thus, the forcing due to the Stokes drift plays a dominant role in the merging of Langmuir cells.

#### *b. Development of the velocity field*

To understand the cell-generation process and, in particular, the amplification of the downwind current anomaly, we study the linearized momentum equation for the

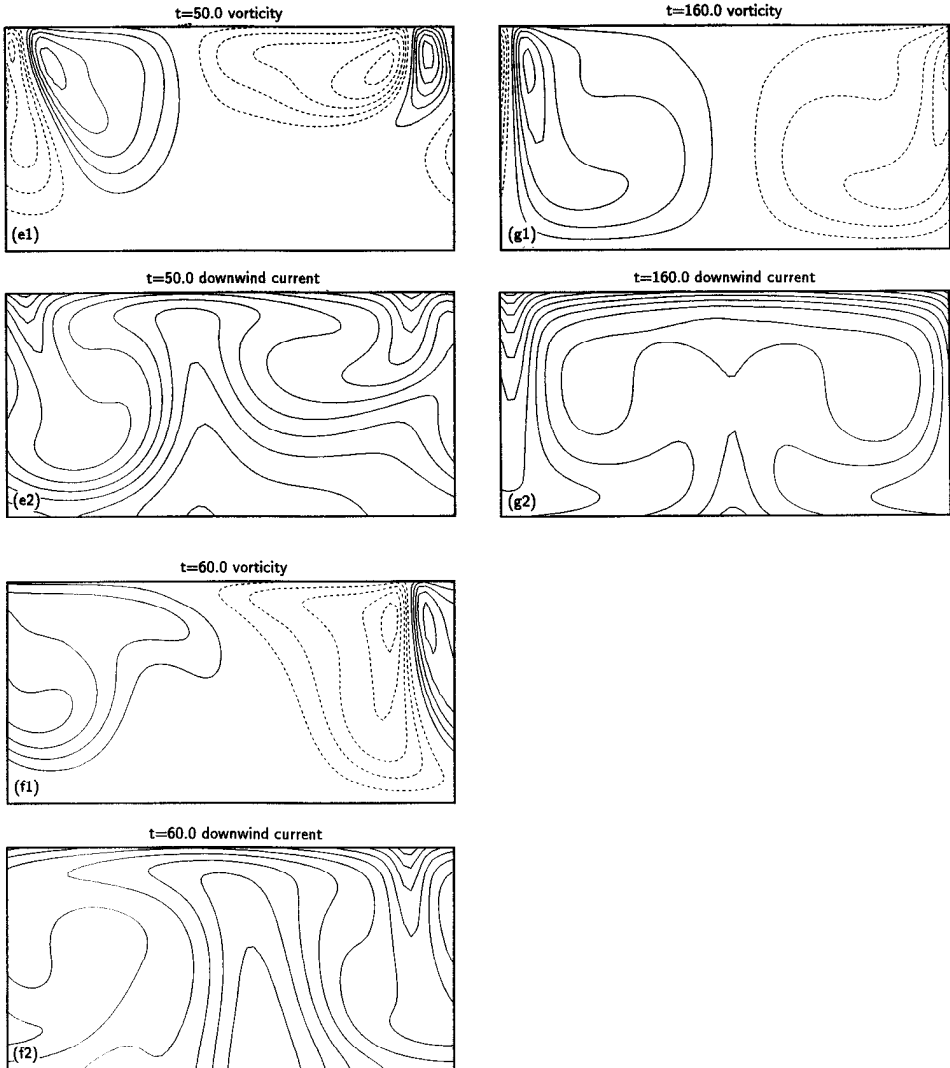


Figure 1. (Continued)

perturbation current  $u' = u - U(z, t)$ ,

$$\frac{\partial u'}{\partial t} = -w \frac{\partial U}{\partial z} + La \nabla^2 u' \tag{25}$$

where  $\partial U / \partial z > 0$ . The viscous term  $La \nabla^2 u'$  is much smaller than the advection term  $-w \partial U / \partial z$  except near the surface. Since  $-w \partial U / \partial z > 0$  at the downwelling site and  $-w \partial U / \partial z < 0$  at the upwelling site,  $u'$  will increase with time beneath the surface

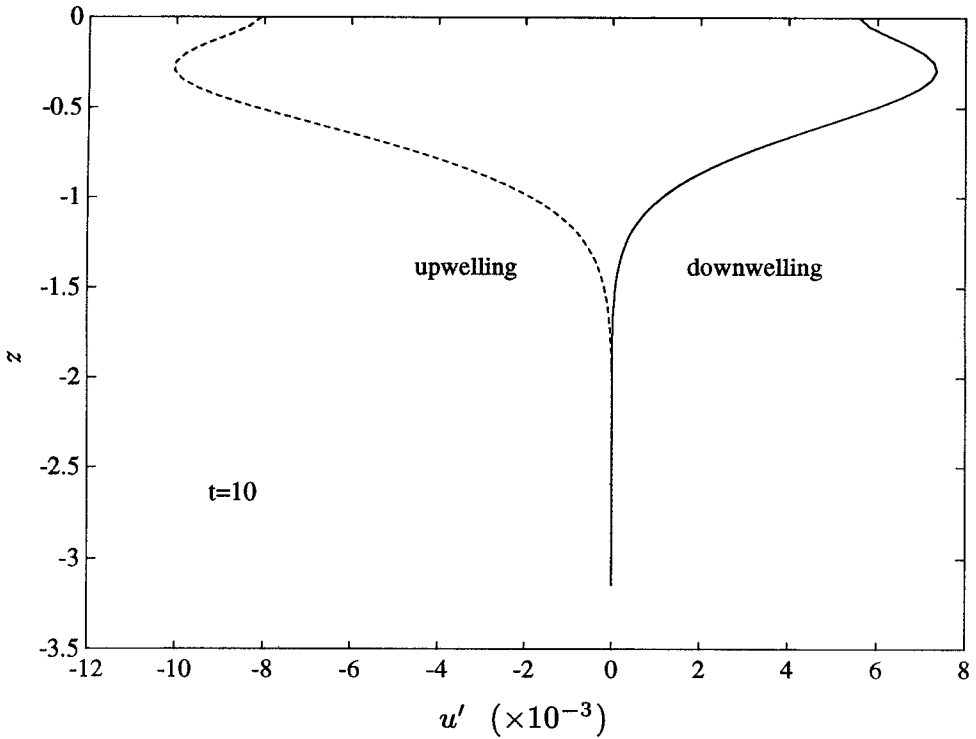


Figure 2. Vertical profiles of the perturbation downwind velocity component at upwelling and downwelling sites at  $t = 10$ .

convergence zone but decrease with time beneath the surface divergence zone. At  $t = 10$ , the perturbation downwind current has a subsurface maximum at the downwelling site and a subsurface minimum at the upwelling site (Fig. 2). The profile of the surface perturbation current is shown in Figure 3.

At the water surface, where  $w = 0$ , Eq. (25) becomes

$$\frac{\partial u'}{\partial t} = La \left( \frac{\partial^2 u'}{\partial y^2} + \frac{\partial^2 u'}{\partial z^2} \right). \tag{26}$$

At the convergence line, the model shows  $\partial^2 u' / \partial y^2 < 0$  and  $\partial^2 u' / \partial z^2 > 0$ , while  $\partial^2 u' / \partial y^2 > 0$  and  $\partial^2 u' / \partial z^2 < 0$  at the divergence line (compare Figs. 2 and 3). At early stages the derivative in the  $z$  direction is necessarily greater than that in the  $y$  direction, because of the vertical transfer of  $u'$  by  $w$ . Hence  $\partial u' / \partial t > 0$  at the convergence line and  $\partial u' / \partial t < 0$  at the divergence line, so that the surface-current anomaly is amplified. In physical terms, the surface downwind jet is reinforced because the frictional resistance is less at the downwelling site than at the upwelling site.

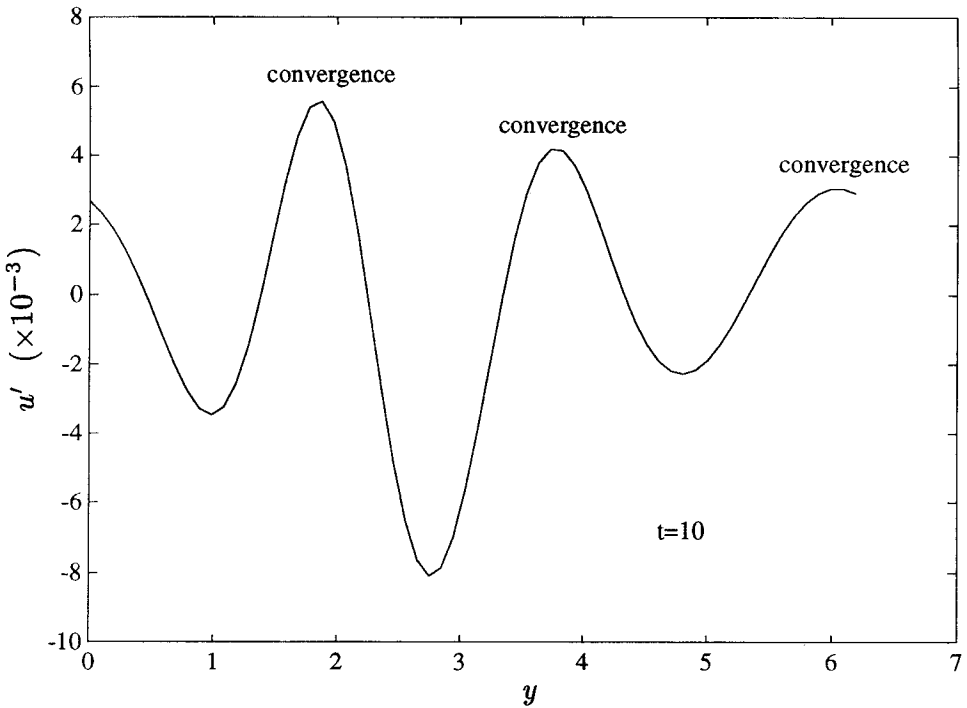


Figure 3. Perturbation surface current at  $t = 10$ .

As the surface current anomaly further increases, the  $y$  derivative becomes comparable with the  $z$  derivative. Furthermore, the nonlinear term  $v(\partial u' / \partial y)$  becomes important and always makes a negative contribution to  $\partial u' / \partial t$ . The perturbation surface current then becomes increasingly negative (Fig. 4) because the horizontal momentum is transferred to the underlying current by the cells. The wind stress that supplies the momentum to the current is fixed and so is the growth of the total downwind momentum. If more momentum is transported downward, the perturbation downwind current at the surface must decrease. In Figure 5, we show profiles of the total downwind current averaged across the cells. At  $t = 20$  it is less steep than  $U(z, t)$ , and at  $t = 40$  a portion of the profile becomes homogeneous. As cells penetrate deeper into the water, the downwind current becomes uniform over greater depths. Except near the surface, the downwind current becomes vertically uniform from  $t = 60$  onward.

As an indicator for the evolution of the cells, we plot the time series of the kinetic energy consisting of  $y$  and  $z$  velocity components (Fig. 6). As instability sets in, the energy increases exponentially. The energy then oscillates for a few cycles before settling down to a constant level for  $t > 100$ , suggesting that a quasi-steady state is established.

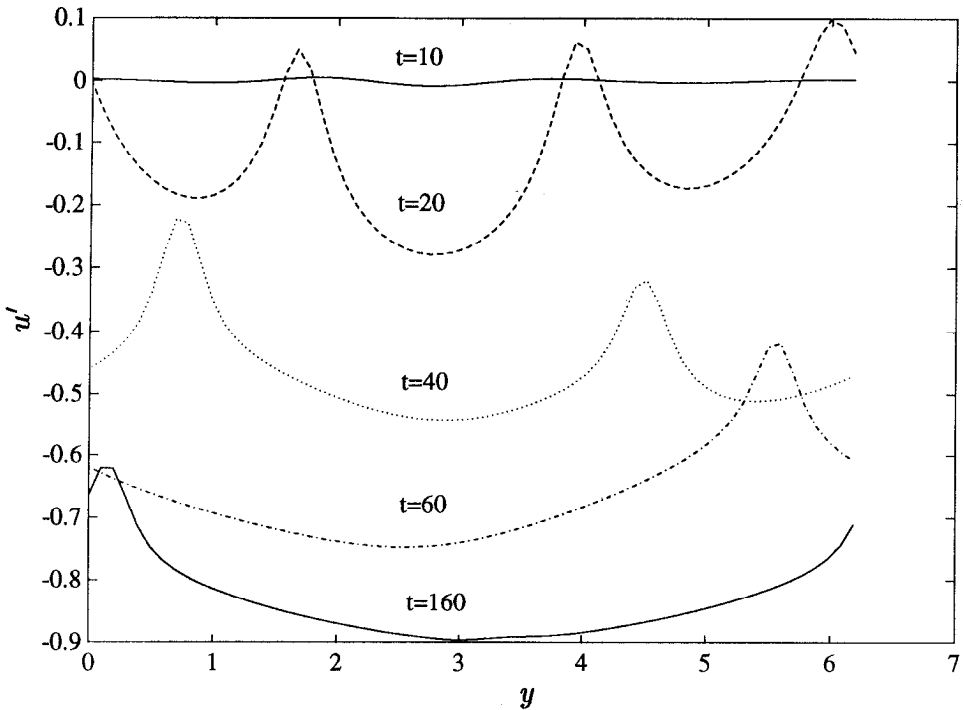


Figure 4. Evolution of the perturbation surface current.

### c. The final quasi-steady state

Flows in the quasi-steady cells are shown in Figures 1(g1) and 1(g2). Away from the downwelling site, isolines of the total downwind velocity  $u = U + u'$  are horizontal and the high shear is concentrated near the surface, indicating a surface boundary layer. Right at the narrow downwelling zone, however, the downwind-velocity isolines become nearly vertical except in the top corner. Within the corner region where the surface boundary layer and the downwelling site overlap, the downwind-velocity isolines make an angle of approximately  $45^\circ$  with the horizontal direction, implying the velocity shear has comparable  $y$  and  $z$  components.

In addition to the contour diagrams, vertical and horizontal velocity profiles are plotted to further illustrate the properties of the steady convective cells. Figure 7 shows the downwind-current profiles at the upwelling and downwelling sites. The existence of the boundary layer at a small Langmuir number is demonstrated in the downwind-current profile at the upwelling site with a sharp velocity gradient close to the surface and an almost homogeneous profile down below. In contrast, the downwind current at the downwelling site has a shear penetrating deeper into the water, although evidently even this profile is less steep than the wind-driven current  $U(z, t)$  without the cells. To reveal the flow structure at the downwelling site, we have

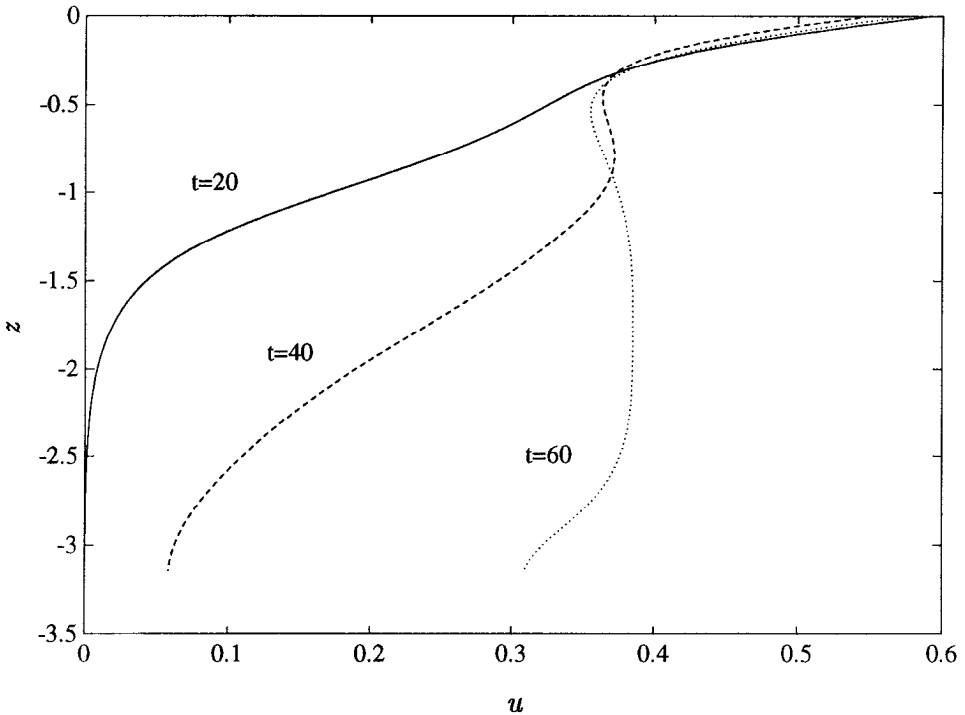


Figure 5. Evolution of the averaged downwind current.

plotted a profile of the perturbation surface downwind jet at  $t = 160$  in Figure 4. The downwind perturbation velocity increases steadily as a water particle is swept away from the divergence line. But there is a rapid jump of the downwind velocity within the narrow region at the convergence zone, because friction is reduced there.

Figure 8 shows that the downwelling velocity is significantly larger than the upwelling velocity as a consequence of the asymmetry of the cells.

*d. Flow indices*

We now examine the maximum downwelling velocity

$$\tilde{w}_{dn} = u_* \left( \frac{S_0}{u_*} \right)^{1/3} La^{-1/3} w_{dn} \tag{27}$$

and the ratio of surface downwind jet strength to the maximum downwelling velocity

$$Pt = \frac{\tilde{u}_{con} - \tilde{u}_{div}}{\tilde{w}_{dn}} = \left( \frac{S_0}{u_*} \right)^{-2/3} La^{-1/3} \frac{u_{con} - u_{div}}{w_{dn}} \tag{28}$$

as functions of  $La$ .

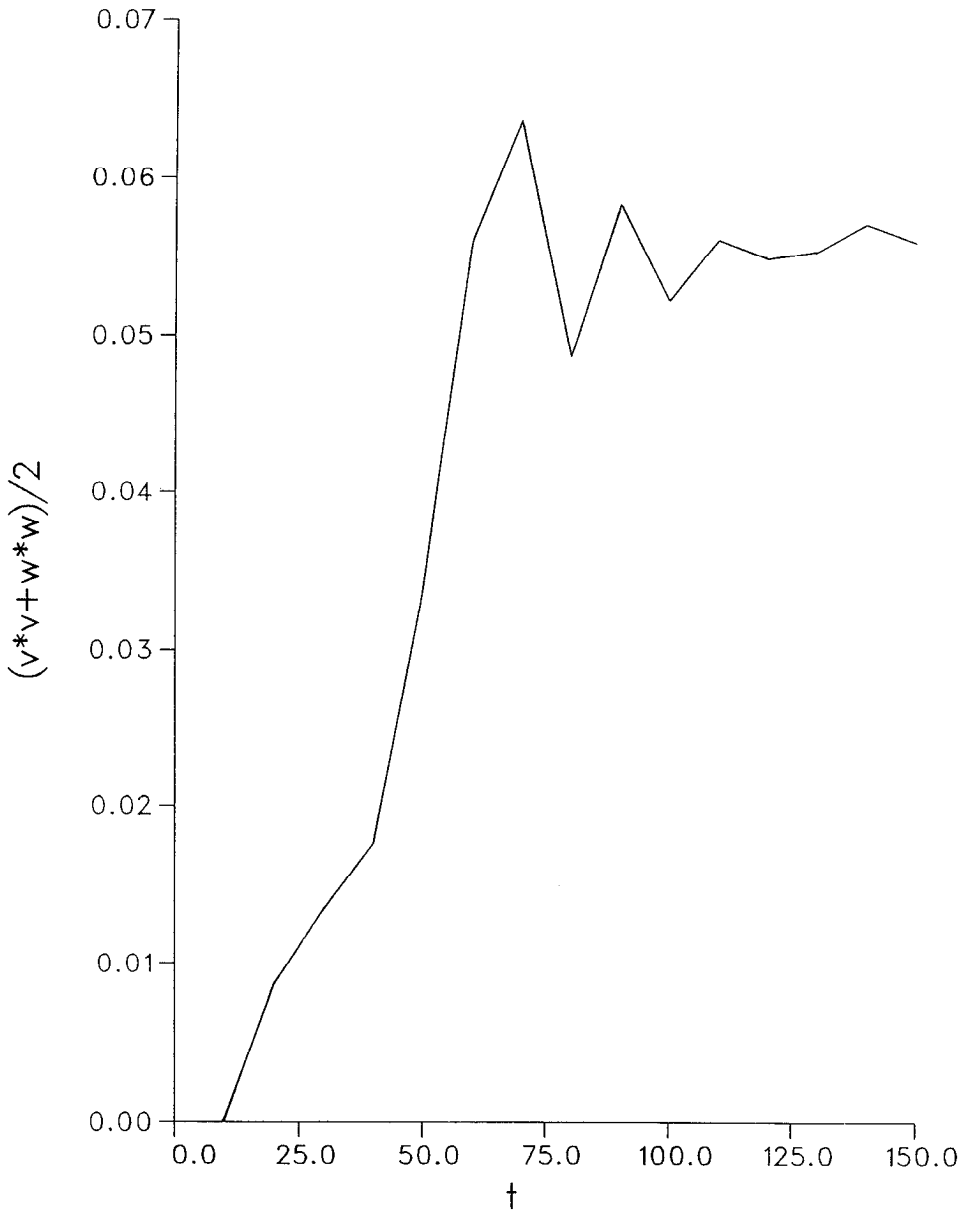


Figure 6. Time series of the cross-wind kinetic energy.

The downwelling velocity increases as  $La$  decreases (Fig. 9), and is proportional to  $La^{-1/3}$  at small Langmuir numbers. The pitch  $Pt$  decreases with  $La$  (Fig. 10) and at a rate for small  $La$  not inconsistent with the power law  $La^{1/6}$  which we shall later derive from a scaling analysis. The trend implies that as viscosity decreases the growth of the downwind jet cannot keep up with the increase of the vertical velocity, presumably

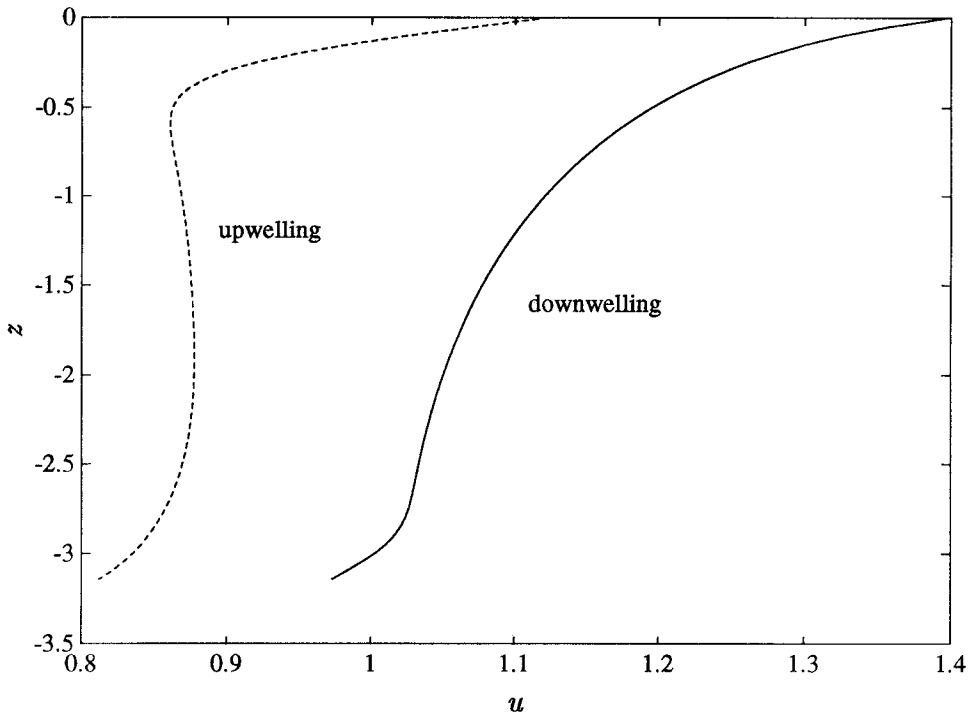


Figure 7. Vertical profiles of the total downwind current at downwelling and upwelling sites for quasi-steady cells.

because the Stokes drift can more effectively transform vertical vorticity into streamwise vorticity when the friction is reduced.

The form of  $U(z, t)$  does not influence the vertical velocity significantly, as shown in Figure 9. For the same magnitude of the downwelling velocity, the surface downwind jet is stronger for the steady Couette flow than for the developing basic current (Fig. 10). The gap between the two is indistinguishable at larger values of  $La$  but widens at small  $La$ . This gap is caused by the difference of  $dU/dz$ , between the two forms of the basic current, which becomes larger at smaller values of  $La$ .

In Figure 11, we show how the width of the surface downwind jet varies with the Langmuir number. Since the surface jet profile does not look like a spike, it is difficult to define the jet width. By comparing the surface jet profiles at different values of  $La$ , we find that the increment of the downwind jet always takes two steps with similar magnitude, one over a broad distance and the other over a narrow region at the convergence zone. The subjectively estimated width of this narrow region increases with Langmuir number, but the lack of precision of the estimate presumably accounts for the departure from the  $La^{1/2}$  law, which, again, we will later derive from a scaling analysis.

Figure 12 shows the time series of the maximum downwelling velocity and pitch for  $La = 0.02$ . Both  $\bar{w}_{dn}$  and  $Pt$  fluctuate before approaching constant limits. The high

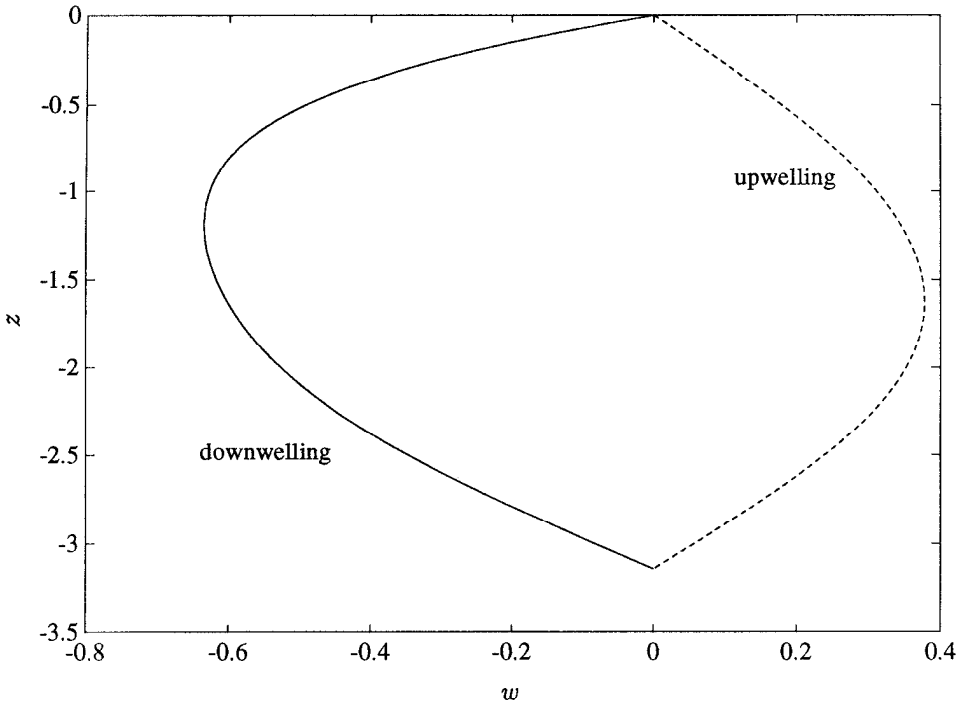


Figure 8. Vertical profiles of the downwelling and upwelling velocities for quasi-steady cells.

pitch corresponds to very low downwelling velocity; both  $\bar{w}_{dn}$  and  $Pt$  are close to their respective asymptotic values when the cells have a finite circulation strength.

**6. Scaling laws at small  $La$**

The numerical results presented in Section 5 have shown that, when Langmuir cells reach a quasi-steady state, the maximum downwelling velocity and the pitch obey power laws at small  $La$ . These power laws can provisionally be explained by a simple scale analysis.

We base our analysis on the steady-state nondimensionalized governing equations

$$v \frac{\partial u'}{\partial y} + w \left( \frac{\partial u'}{\partial z} + \frac{dU}{dz} \right) = La \nabla^2 u', \tag{29}$$

$$v \frac{\partial \Omega}{\partial y} + w \frac{\partial \Omega}{\partial z} = La \nabla^2 \Omega - \frac{du_s}{dz} \frac{\partial u'}{\partial y}, \tag{30}$$

$$v = - \frac{\partial \psi}{\partial z}, \quad w = \frac{\partial \psi}{\partial y}, \quad \Omega = \nabla^2 \psi, \tag{31}$$

where  $dU/dz = 1$  for the steady Couette flow and  $dU/dz = \text{erfc}(-z/(2\sqrt{La t}))$  for the developing flow. The length scales in the  $y$  and  $z$  directions are denoted by  $Y$  and  $Z$ ,

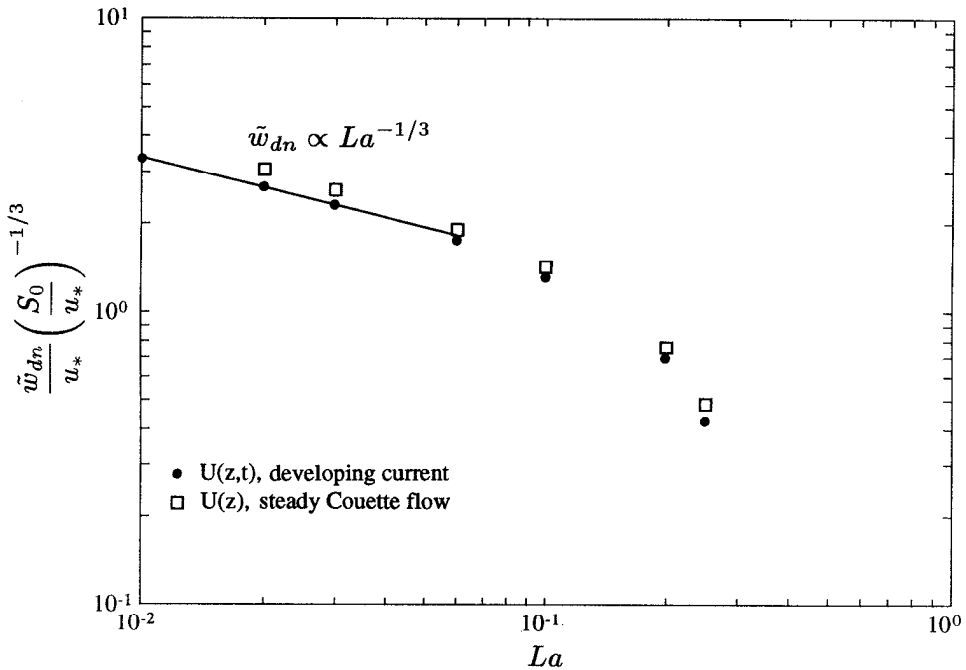


Figure 9. Maximum dimensional downwelling velocity  $\tilde{w}_{dn}$  versus  $La$ .

respectively;  $\Psi$  is chosen to represent the scale for stream function  $\psi$ ,  $W$  is the scale of the downwelling velocity and  $U'$  is the scale of the perturbation downwind current  $u'$ .

As  $La$  goes to zero, the viscous term becomes negligible except near a boundary or in a high-shear region. Since the wind stress applied at the water surface drives the current, friction must be important in a thin surface boundary layer. A second high-shear region can be recognized in the numerical output, such as Figure 1(g1) which shows that the downwind jet is confined near the convergence line for a small Langmuir number. The vorticity is also largely confined to these boundary layers at the surface and beneath the surface convergence line. We divide the flow field into four regions, as shown in Figure 13. Region 1 is the narrow downwelling zone, region 2 denotes the boundary layer below the surface and region 3 is the corner region where regions 1 and 2 overlap. Region 4 is the interior which appears to be purely advective.

*a. The narrow downwelling zone*

Within the narrow downwelling zone, the length scale in the  $y$  direction is much smaller than in the  $z$  direction, so that the viscous term is dominated by the horizontal component i.e.  $\partial^2/\partial y^2 \gg \partial^2/\partial z^2$ . We hypothesize that the advective, diffusive and forcing terms are of the same order of magnitude.

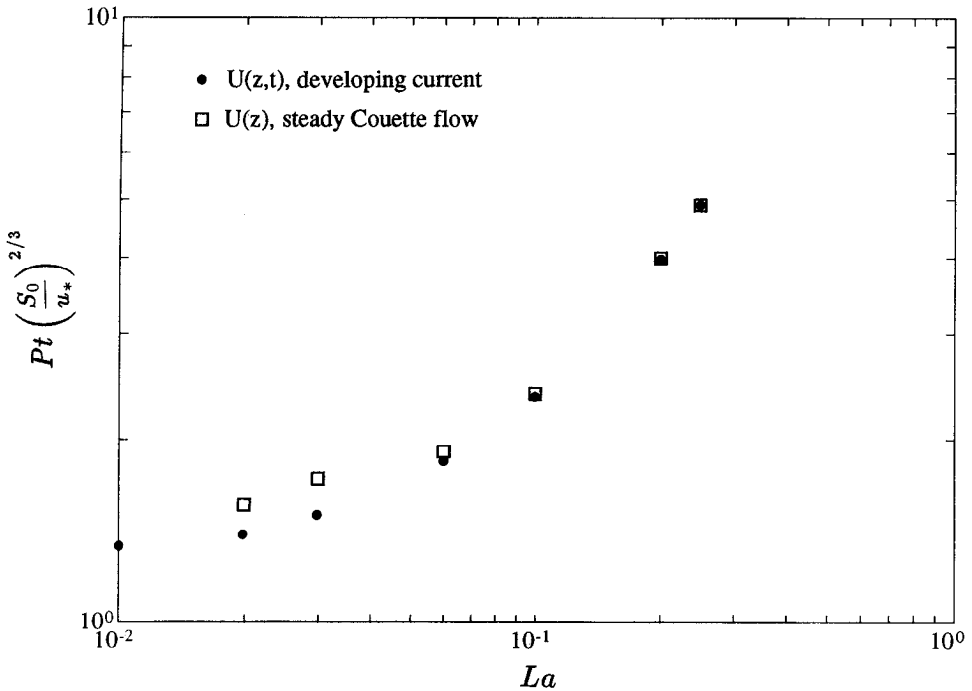


Figure 10. The pitch  $Pt$  as a function of  $La$ .

Equating advection and diffusion terms in (29) and (30) gives

$$\Psi = \frac{LaZ}{Y}. \tag{32}$$

Balancing advection terms and forcing terms in (29) yields

$$U' = Z = O(1), \tag{33}$$

and, using (32), the same balance in (30) gives

$$\frac{La^2Z}{Y^5} = \frac{U'}{Y}. \tag{34}$$

Combining these relations, and taking the dimensionless vertical scale as 1, we have

$$\Psi = La^{1/2}, \tag{35}$$

$$W = 1, \tag{36}$$

$$Y = La^{1/2}. \tag{37}$$

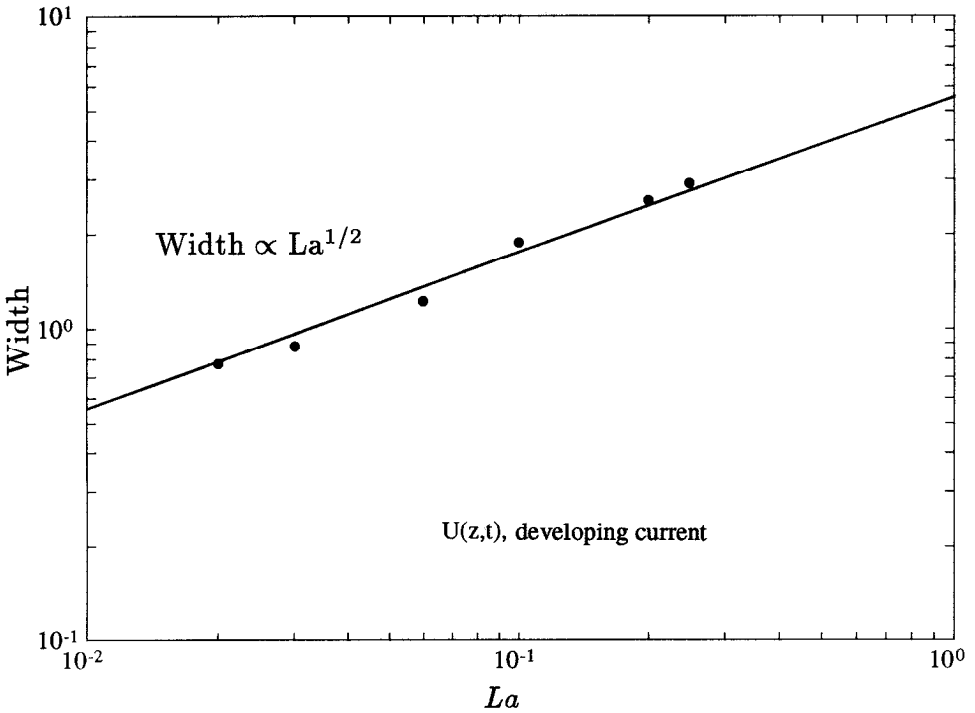


Figure 11. The width of the downwind jet as a function of  $La$ .

Using (8), we can infer for the dimensional downwelling velocity

$$\bar{w}_{dn} \propto La^{-1/3}, \tag{38}$$

in excellent agreement with the empirical formula obtained from the numerical model.

The prediction that the width of the downwind jet decreases with Langmuir number as  $La^{1/2}$  is also consistent with the numerical results at small  $La$  (Fig. 11).

*b. The surface boundary layer*

In the surface boundary layer (region 2, Fig. 13) viscous diffusion is dominated by the  $z$  component,  $\partial^2/\partial z^2 \gg \partial^2/\partial y^2$ .

If advection and diffusion terms are of the same order of magnitude, we have

$$\Psi = \frac{LaY}{Z}, \tag{39}$$

whence

$$Z = (\beta L)La^{1/2}, \tag{40}$$

by virtue of (35) and if we take  $Y = \beta L$  as the horizontal scale.

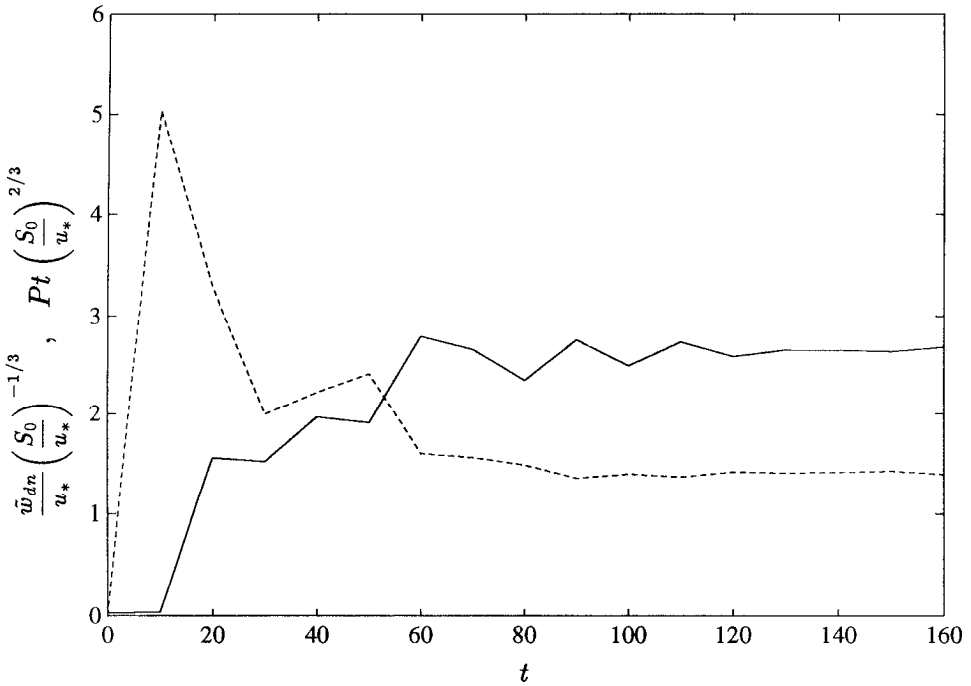


Figure 12. Time series of  $\bar{w}_{dn}$  and  $Pt$  for  $La = 0.02$ ,  $\beta L = 2\pi$  and  $\beta d = \pi$ . The solid line represents  $\bar{w}_{dn}$  while the dashed line represents  $Pt$ .

Comparability of advection and forcing terms in Eq. (29) gives

$$U' = Z = (\beta L)La^{1/2}, \tag{41}$$

whereas the ratio of advection and forcing terms in (30) is  $La$ , implying that the generation of new vorticity is small in region 2 and that the circulation is mostly generated at the downwelling site. Eq. (41) implies that the downwind velocity increase across region 2 is proportional to the width of the cells.

Eq. (41) shows that the difference in the nondimensional downwind jet between the divergence line and a point just outside the corner region is proportional to  $La^{1/2}$ . Continuing to the convergence line requires consideration of the corner, region 3, where every term in the governing equations must be considered and we do not have a simple scaling argument. However, our numerical output shows that the gain in the downwind velocity at the surface takes two steps with similar magnitude; the drop over the corner in region 4 is approximately the same as in region 2, being of order  $O(La^{1/2})$ . Hence we can argue that the dimensionless jet strength, and pitch, vary as  $La^{1/2}$ . Using (28), the dimensional pitch is proportional to  $La^{1/6}$ , again consistent with our numerical results.

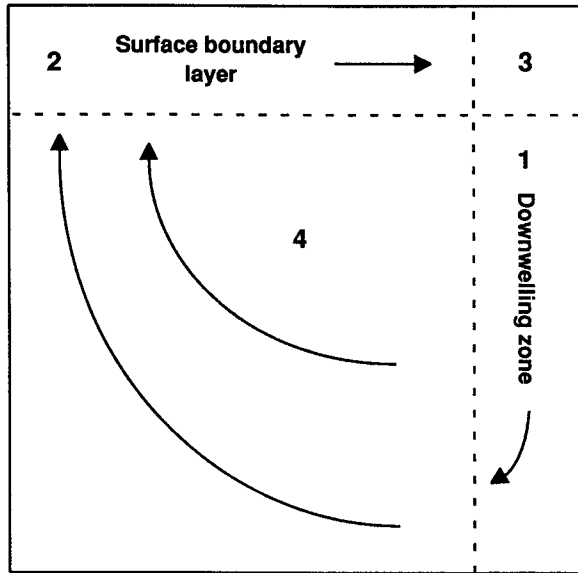


Figure 13. A schematic diagram of the four sub-regions within a cell.

*c. Horizontally variable eddy viscosity*

In the Craik-Leibovich model, the eddy viscosity is assumed to be constant throughout the cells. This raises the question as to whether quantities such as the pitch are sensitive to spatial variations in the strength of the mixing. For a preliminary investigation of this, we extend our scaling analysis to the case where the eddy viscosity  $\nu_1$  at the downwelling site is different from  $\nu_2$  in the surface boundary layer. Incidentally,  $\nu_1$  may be seen as the horizontal eddy viscosity and  $\nu_2$  the vertical eddy viscosity. We now use the dimensional governing equations

$$\bar{v} \frac{\partial \bar{u}'}{\partial \bar{y}} + \bar{w} \left( \frac{\partial \bar{u}'}{\partial \bar{z}} + \frac{u_*^2}{\nu_T} \right) = \nu_T \nabla^2 \bar{u}', \tag{42}$$

$$\bar{v} \frac{\partial \tilde{\Omega}}{\partial \bar{y}} + \bar{w} \frac{\partial \tilde{\Omega}}{\partial \bar{z}} = \nu_T \nabla^2 \tilde{\Omega} - \frac{d\bar{u}_s}{d\bar{z}} \frac{\partial \bar{u}'}{\partial \bar{y}}, \tag{43}$$

$$\bar{v} = - \frac{\partial \tilde{\Psi}}{\partial \bar{z}}, \quad \bar{w} = \frac{\partial \tilde{\Psi}}{\partial \bar{y}}, \quad \tilde{\Omega} = \nabla^2 \tilde{\Psi}. \tag{44}$$

Let  $Y, Z$  denote the horizontal and vertical length scales and  $\Psi, U', W$  represent the scales for the stream function, perturbation downwind current and the downwelling velocity, respectively. Subscripts 1 and 2 are used to indicate regions 1 and 2.

In region 1, comparability of advective and diffusive terms gives

$$\Psi_1 = \frac{\nu_1 Z_1}{Y_1}, \quad (45)$$

while comparability of the advective and forcing terms leads to

$$U'_1 = Z_1 \frac{u_*^2}{\nu_1}, \quad (46)$$

$$\frac{\Psi_1^2}{Z_1 Y_1^3} = (\beta S_0) \frac{U'_1}{Y_1}. \quad (47)$$

From these equations we can deduce

$$Y_1 = \left( \frac{\nu_1^3}{\beta S_0 u_*^2} \right)^{1/4}, \quad (48)$$

$$\Psi_1 = \left( \frac{\nu_1 S_0 u_*^2}{\beta^3} \right)^{1/4}, \quad (49)$$

$$W = \left( \frac{S_0}{\nu_1 \beta} \right)^{1/2} u_*, \quad (50)$$

where we have taken  $\beta^{-1}$  for the depth scale  $z$ . Thus the downwelling velocity is inversely proportional to  $\nu_1^{1/2}$ . If the eddy viscosity at the downwelling region is reduced, the downwelling velocity will increase.

Next we study region 2, the surface boundary layer. Comparability of advection and diffusion terms gives

$$\Psi_2 = \frac{\nu_2 Y_2}{Z_2}, \quad (51)$$

whence

$$Z_2 = \nu_2 L \left( \frac{\beta^3}{\nu_1 S_0 u_*^2} \right)^{1/4} \quad (52)$$

if, as before, we assume that  $\Psi_2 = \Psi_1$ , and take  $L$  as the horizontal length scale. Matching advection and forcing in (42) gives

$$U'_2 = \frac{u_*^2}{\nu_2} Z_2 = u_* L \left( \frac{\beta^3 u_*^2}{\nu_1 S_0} \right)^{1/4} \quad (53)$$

independent of  $v_2$ . Combining the scales for the downwind jet and the downwelling velocity, we obtain

$$\frac{U'_2}{W} = \beta L \left( \frac{v_1 \beta u_*^2}{S_0^3} \right)^{1/4} \quad (54)$$

which is also independent of  $v_2$ . Thus, the pitch is unaffected by  $v_2$  if we assume that the  $u$  increment in the corner region is also independent of  $v_2$ .

## 7. Comparison between model predictions and observations

### a. Observations

Comprehensive measurements were made at sea from the Research Platform, FLIP, by Weller and Price (1988) and Smith *et al.* (1987). They found downward vertical and downwind horizontal velocity components significantly larger than previously reported. The downwind, downwelling flow was jet-like in structure and was confined to relatively narrow regions that coincided with bands of convergent surface flow. At mid-depth in the mixed layer, the downwelling flow had a maximum velocity of  $0.3 \text{ m s}^{-1}$  and was accompanied by a downwind, horizontal jet of comparable magnitude, about  $0.4 \text{ m s}^{-1}$ . Thus, the net fluid velocity under the windrows is directed downward about  $45^\circ$  at mid-depth in the mixed layer. Away from the downwelling regions and in the lower half of the mixed layer below the convergence zones, the flow associated with the Langmuir cells was an order of magnitude smaller and not well resolved in the experiments.

### b. Downwelling velocity

Leibovich (1983) suggested a simple linear relation

$$\tilde{w}_{dn} \approx 0.0085 U_w \quad (55)$$

between the observed downwelling velocities and the wind speed. With  $La = 0.01$ , we find using (19) that the CL2 model gives for the maximum downwelling velocity

$$\tilde{w}_{dn} \approx 0.006 \text{ to } 0.01 U_w. \quad (56)$$

In the FLIP observations, the wind speed  $U_w$  varied between  $5$  and  $15 \text{ m s}^{-1}$ . At  $La = 0.01$  the CL2 model predicts  $\tilde{w}_{dn} = 0.03$  to  $0.15 \text{ m s}^{-1}$ , being in the range of observed downwelling velocity of  $0.03$  to  $0.27 \text{ m s}^{-1}$ . For smaller values of  $La$ , the CL2 model will give an even bigger downwelling velocity. In Section 3 we showed that for  $La = 0.001$  to  $0.01$  the eddy viscosity is in the range of values commonly used for the ocean surface layer. Thus it appears that by choosing an appropriate value for the eddy viscosity, the CL2 model can provide the right prediction for the downwelling velocity.

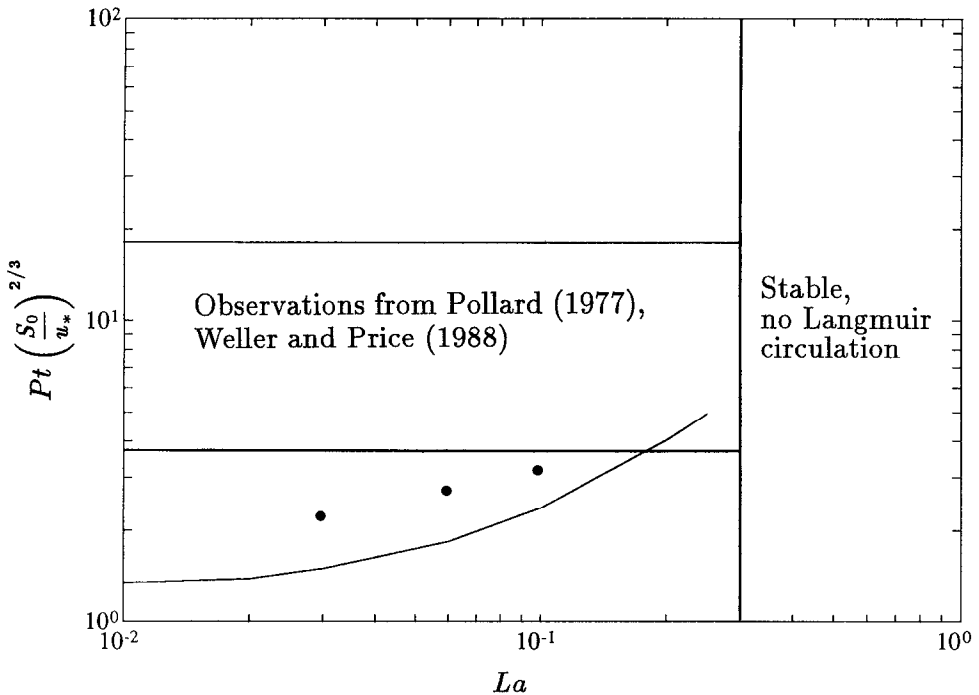


Figure 14. A comparison of model predictions and observations for the pitch.  $\beta L = 2\pi$ ,  $\beta d = \pi$  for the solid curve and  $\beta L = 4\pi$ ,  $\beta d = \pi$  for dotted points.

### c. Pitch

The CL2 model and observations appear to disagree, however, with respect to the pitch, the ratio of the surface downwind jet strength to the maximum downwelling velocity. In Pollard's (1977) diagram, the downwind current at the convergence zone relative to that at the divergence zone is about  $0.1 \text{ m s}^{-1}$ , while the downwelling velocity varies between  $0.02$  and  $0.06 \text{ m s}^{-1}$ . Thus the pitch  $Pt$  has a value of  $1.7$  to  $5$ . The older Langmuir circulation data summarized by Pollard may not be reliable for forming  $Pt$ , because few of the early studies were made to capture the maximum downwelling. Recent observations by Weller and Price (1988) found a downwelling velocity of up to  $0.3 \text{ m s}^{-1}$ , although smaller velocities in the range of  $0.05$  to  $0.1 \text{ m s}^{-1}$  were more frequently recorded. The maximum horizontal velocity measured below the surface was  $0.4 \text{ m s}^{-1}$ , which is used as a rough estimate for the surface downwind jet strength. Thus Weller and Price's observations suggest a pitch about  $1.33$ , but it can be as high as  $8$  if smaller values of downwelling velocity are used. The CL2 model, however, predicts a pitch between  $0.37$  and  $0.49$ , about one third of the observed strength or less for  $La = 0.01$ , at which the right range of downwelling velocity can be predicted. In other words, the CL2 model predicts a downwind current strength appreciably less than the downwelling velocity. Figure 14 shows the comparison

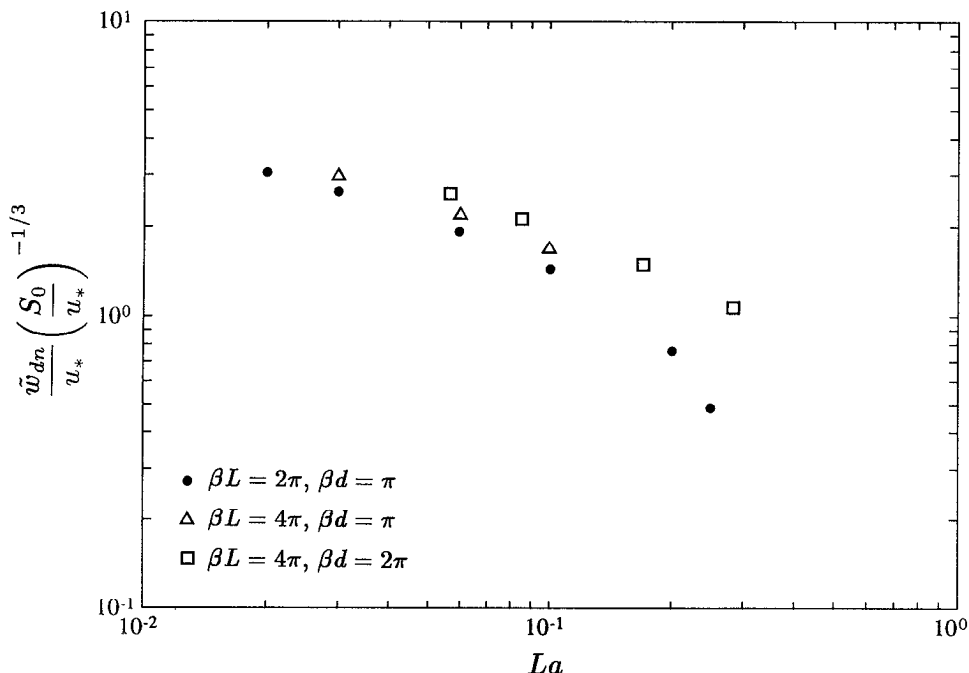


Figure 15. Comparison of the downwelling velocity  $w_{dn}$  for different values of  $\beta L$  and  $\beta d$ .

between observed and predicted pitch. In the figure the solid curve is a direct output from the numerical model (three solid points above the curve correspond to cells with an aspect ratio of 2 and will be discussed in the next section), but for observations we calculate the pitch from Pollard's or Weller and Price's measurements and combine it with the estimate of  $S_0/u_*$  given in (19). Uncertainty in estimating the Stokes drift and friction velocity as well as calculating velocity components all contribute to a broad band defined by the data.

As a summary of the comparison with observations, the CL2 model appears to predict a weaker downwind jet and the shape of the downwind jet is not pronounced.

#### d. Dependence of $\bar{w}_{dn}$ and $Pt$ on $\beta L$ and $\beta d$

For Langmuir circulations formed in a deep and homogeneous ocean, we have two dimensionless parameters  $La$  and  $S_0/u_*$ . In the numerical model there are two additional parameters,  $\beta L$  and  $\beta d$ , which describe the horizontal and vertical scales of the box, respectively. Our standard numerical runs are carried out in a box with  $\beta d = \pi$  and  $\beta L = 2\pi$ . Now we want to check how  $\bar{w}_{dn}$  and  $Pt$  vary with  $\beta L$  and  $\beta d$ . In these numerical tests we take the basic current  $U(z)$  to be the Couette flow.

First we double the horizontal extent, i.e. choose a box with  $\beta L = 4\pi$  and  $\beta d = \pi$ . For the same  $La$ , more cells are observed in this wider box as instability sets in. The

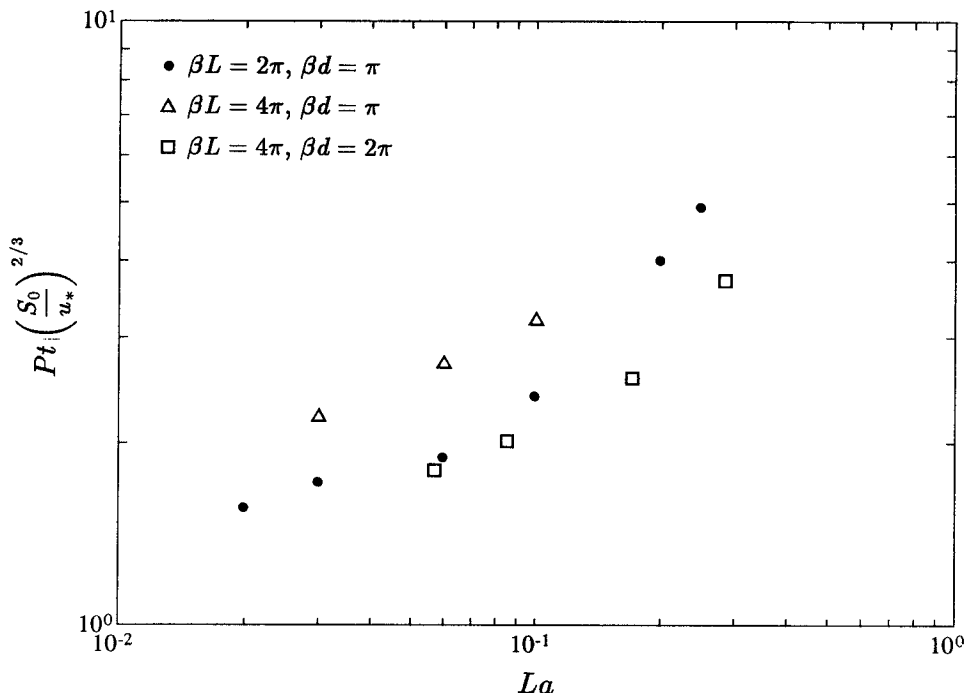


Figure 16. Comparison of the pitch  $Pt$  for different values of  $\beta L$  and  $\beta d$ .

cells merge with each other and approach a quasi-steady state when a pair of flat cells with an aspect ratio of 2 is left. The maximum downwelling velocity  $\bar{w}_{dn}$  remains almost the same, although  $Pt$  is bigger for the flat cells (Figs. 15 and 16). As predicted by (41), the surface downwind jet (Fig. 17) is stronger because a water particle is exposed to the wind stress for a longer time as it moves across a greater distance from the divergence line to the convergence line. Figure 17 also suggests that the width of the downwelling region does not vary with  $\beta L$ .

Next we double both the horizontal and the vertical dimensions of the computation box, i.e. choose  $\beta L = 4\pi$  and  $\beta d = 2\pi$ . At small  $La$  both  $\bar{w}_{dn}$  and  $Pt$  converge to those of the standard runs at small  $La$  (see Figs. 15 and 16). The downwelling velocity  $\bar{w}_{dn}$  does not vary significantly with  $\beta d$ , but the pitch drops by a half when  $\beta d$  is doubled.

In the FLIP observations the maximum wind speed was about  $15 \text{ m s}^{-1}$  and the maximum horizontal cell size stayed close to 1.5 times the mixed layer depth as the depth varied from 40 to 60 m. At wind speed of  $15 \text{ m s}^{-1}$ , the  $e$ -folding depth of the Stokes drift is  $1/(2\beta) = 2.76 \text{ m}$  (according to (20)). The quasi-steady cells shown in our standard runs thus have a horizontal scale of  $\frac{1}{2}L = 17 \text{ m}$  and a vertical scale of  $d = 17 \text{ m}$ . The flat cells have a size of  $\frac{1}{2}L = 34 \text{ m}$  and  $d = 17 \text{ m}$ , while the big square cells have  $\frac{1}{2}L = 34 \text{ m}$  and  $d = 34 \text{ m}$ . Therefore the cells simulated in our numerical

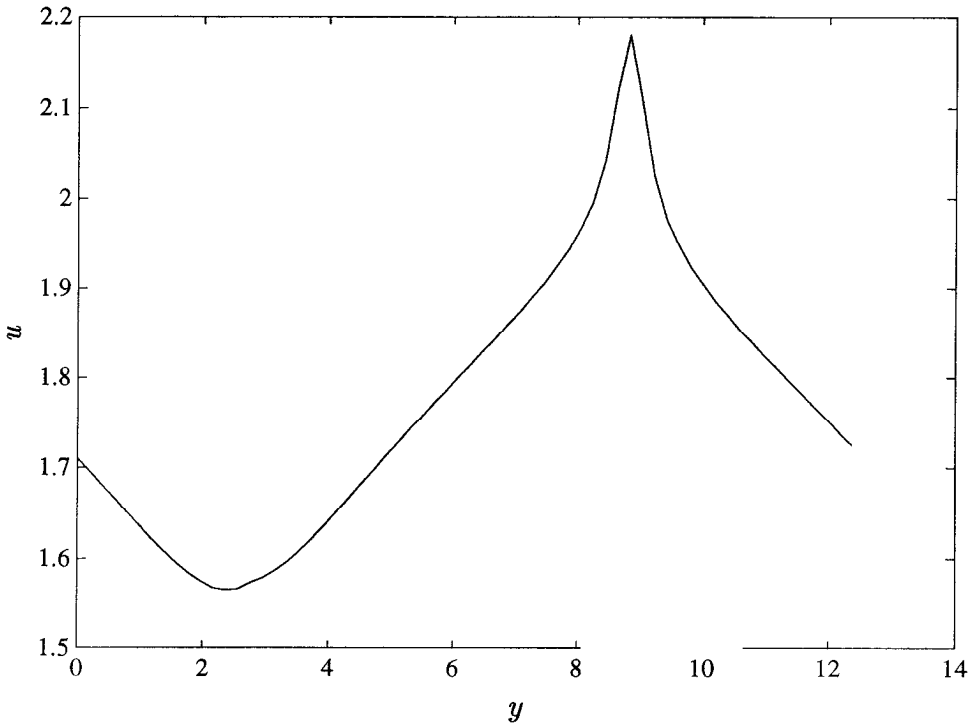


Figure 17. The profile of the surface downwind current for  $La = 0.02$ ,  $\beta L = 4\pi$  and  $\beta d = \pi$ .

model have a size comparable with observed cell size. Although the pitch for the flat cells is closer to the observations than the square cells, the downwind jet has a broad shape which does not match with the sharp jet observed by Weller and Price (1988).

*e. Effects of the Stokes drift profile*

We have used an exponential profile for the Stokes drift current. The Stokes drift current calculated from the Pierson and Moskowitz spectrum, from (15), drops more quickly than an exponential function in a thin surface layer but decreases more gently at lower depths (Fig. 18). To fit this profile, we have chosen a sum of two exponentials, i.e.

$$\tilde{u}_s = 1.0723S_0 \exp(0.4z^*) + 0.9277S_0 \exp(4z^*) \tag{57}$$

where  $z^* = g\bar{z}/U_w^2$ . The surface value and  $e$ -folding depth of this function are the same as calculated from (15).

In Figure 19,  $Pt$  corresponding to (57) is compared with that calculated from the exponential profile. It is found that  $Pt$  is about 20 to 30% larger, with most of the change due to the reduction in  $\tilde{w}_{dn}$ , perhaps due to weaker vorticity forcing at middle depths. The stronger forcing close to the surface is less effective due to high viscous

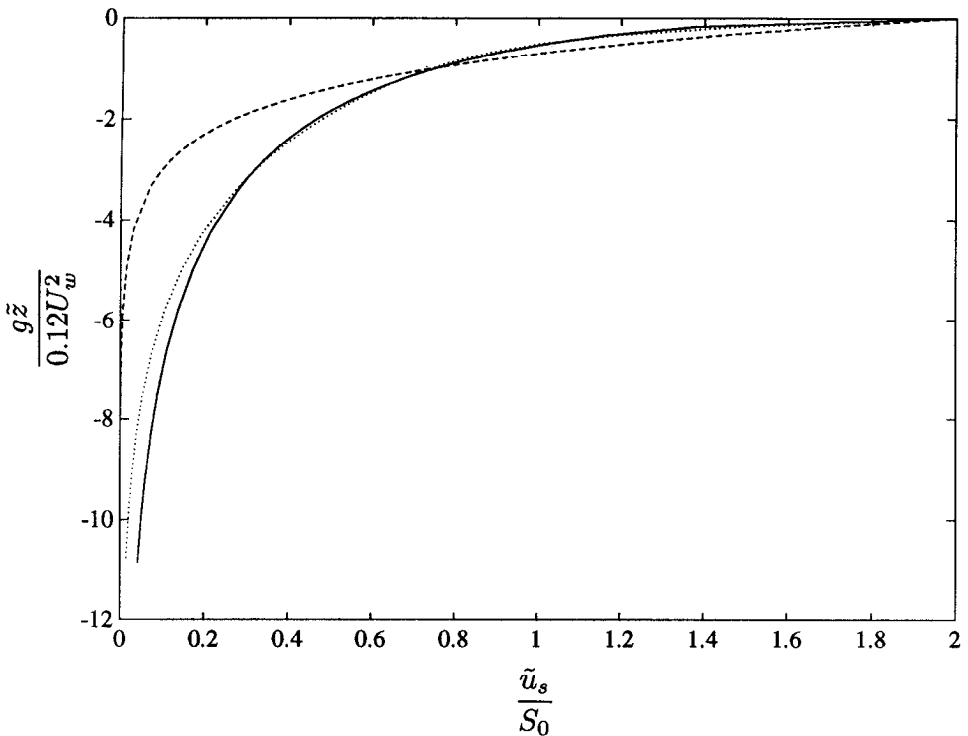


Figure 18. Profiles of the Stokes drift current. Solid curve is from the Pierson and Moskowitz spectrum. The dashed curve represents an exponential profile and the dotted curve is a sum of two exponentials used to fit the solid curve.

dissipation. It is concluded that the profile of the Stokes drift current does not significantly affect the magnitude of the pitch.

## 8. Conclusions

In the numerical simulation counterrotating cells are seen to cancel each other and then approach a quasi-steady state. The quasi-steady cells did not select a definite horizontal scale; our computations are for an aspect ratio  $\frac{1}{2}L/d$  either 1 or 2. However, Smith *et al.* (1987) proposed that the mixed-layer depth might determine the maximum horizontal spacing and that the cell aspect ratio is about 1.5. In addition, Weller and Price (1988) observed that the merging of Langmuir cells is a continuous process and there is in fact a coexistence of multiple cell sizes with the dominant cell size increasing with the wind speed (Zedel and Farmer, 1991). In the numerical simulation we have not seen the regeneration of small cells and their subsequent upscale merging, though we plan experiments in which noise is added to the flow pattern of quasi-steady cells.

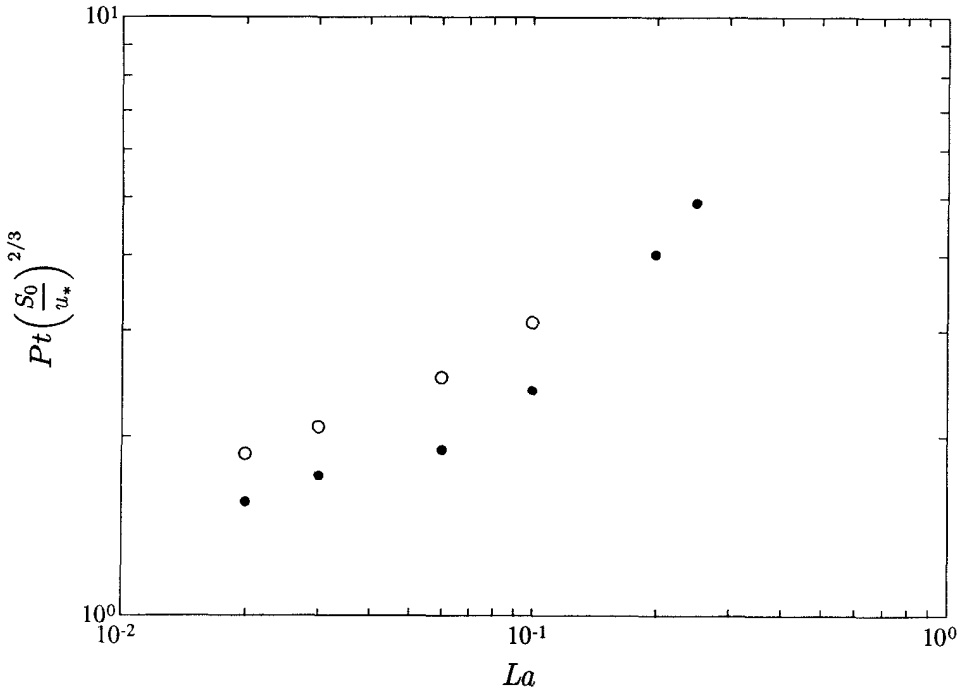


Figure 19. Comparison of  $Pt$  for different Stokes drift profiles. Solid dots correspond to the Stokes drift having an exponential profile. Open circles correspond to the Stokes drift having a profile which is a sum of two exponentials.

An asymptotic regime is found at small Langmuir number in the CL2 model. The flow within a cell consists of a surface boundary layer, a narrow downwelling zone and a purely advective region away from the boundaries. A preliminary scaling analysis predicts power law dependences in accord with numerical results, but further work is required, particularly for the corner region at the surface convergence.

Our comparison shows that the downwind jet strength predicted by the CL2 model is appreciably smaller than the strength reported by Pollard (1977) and Weller and Price (1988). Pollard's diagram is most suitable for the comparison of the pitch, but more recent observations by Weller and Price (1988) have focused on the downwelling velocity and have made no attempt to measure the downwind jet at the water surface. In Section 7 we used the maximum horizontal velocity measured at a depth below the surface as an approximation to the downwind jet strength, for Weller and Price claimed that the horizontal velocity signal is weak in places other than the downwelling site. The downwind jet at a depth below the surface may be stronger or weaker than the surface jet. In order to make a fair comparison with the model predictions, the surface downwind velocity as well as the maximum downwelling

velocity must be measured in future. The wind stress and Stokes drift profile (i.e. the full wave spectrum) are also required.

A weakness of existing models is the use of a constant eddy viscosity to parameterize small-scale turbulent processes. Using scale analysis, we have argued that a horizontally variable eddy viscosity does not affect the magnitude of the pitch. However, a vertically variable eddy viscosity might alter the dynamics of the cells. The commonly accepted form of eddy viscosity is a linearly increasing function of depth, such as used in the atmospheric boundary layer. The ocean surface, which is constantly acted on by wind stress and breaking waves, is a source of turbulence. Hence the eddy viscosity might be a decreasing function of depth rather than an increasing function in a thin subsurface region. Thus a better understanding of small-scale turbulence may be essential in the modelling of larger coherent structures such as Langmuir circulation.

If better observations and further modelling confirm the discrepancy in the downwind jet strength, we then need to look for some other mechanism that can provide the extra forcing required to drive the downwind jet at the convergence zone. This could be preferential dissipation in the jet of short surface waves that are steepened while being refracted (Garrett, 1976). However, the steepening of some waves in a typical wave directional spectrum may be offset by the loss of waves that are internally reflected, resulting in less, rather than more, wave dissipation in the jet (Smith, 1983).

*Acknowledgments.* We are grateful to David Farmer, Leo Maas, Sid Leibovich, Hide Yamazaki and Amit Tandon for stimulating discussions and to Greg Holloway and Dave Ramsden for their help with the spectral code. Thanks are also due to Rosalie Rutka for preparing the diagrams. Financial support from the U.S. Office of Naval Research and Canada's Natural Sciences and Engineering Research Council is gratefully acknowledged.

#### REFERENCES

- Andrews, D. G. and M. E. McIntyre. 1978. An exact theory of nonlinear waves on a Lagrangian-mean flow. *J. Fluid Mech.*, 89, 609–646.
- Canuto, C., M. Y. Hussaini, A. C. Quarteroni and T. A. Zang. 1987. *Spectral Methods in Fluid Dynamics*. Springer-Verlag, Berlin, 567 pp.
- Cox, S. M., S. Leibovich, I. M. Moroz and A. Tandon. 1992. Nonlinear dynamics in Langmuir circulations with  $O(2)$  symmetry. *J. Fluid Mech.*, 241, 669–704.
- Craik, A. D. D. 1977. The generation of Langmuir circulations by an instability mechanism. *J. Fluid Mech.*, 81, 209–223.
- Craik, A. D. D. and S. Leibovich. 1976. A rational model for Langmuir circulations. *J. Fluid Mech.*, 73, 401–426.
- Faller, A. J. and S. J. Auer. 1988. The roles of Langmuir circulations in the dispersion of surface tracers. *J. Phys. Oceanogr.*, 18, 1108–1123.
- Garrett, C. J. R. 1976. Generation of Langmuir circulations by surface waves—a feedback mechanism. *J. Mar. Res.*, 34, 117–130.
- Hasselmann, K., T. P. Barnett, E. Bouws, H. Carlson, D. E. Cartwright, K. Ende, J. A. Ewing, H. Gienapp, D. E. Hasselmann, P. Kruseman, A. Meerburg, P. Muller, D. J. Olbers, K.

- Richter, W. Sell and H. Wladen. 1973. Measurements of wind-wave growth and swell decay during the Joint North Sea Wave Project (JONSWAP). *Dtsch. Hydrogr. Z., Suppl.*, 48, No. 12.
- Huang, N. E. 1971. Derivation of Stokes drift for a deep-water random gravity wave field. *Deep-Sea Res.*, 18, 255–259.
- 1979. On surface drift currents in the ocean. *J. Fluid Mech.*, 91, 191–208.
- Kenyon, K. E. 1969. Stokes drift for random gravity waves. *J. Geophys. Res.*, 74, 6991–6994.
- Langmuir, I. 1938. Surface motion of water induced by wind. *Science*, 87, 119–123.
- Leibovich, S. 1977a. On the evolution of the system of wind drift currents and Langmuir circulations in the ocean. Part 1. Theory and averaged current. *J. Fluid Mech.*, 79, 715–743.
- 1977b. Convective instability of stably stratified water in the ocean. *J. Fluid Mech.*, 82, 561–581.
- 1980. On wave-current interaction theories of Langmuir circulations. *J. Fluid Mech.*, 99, 715–724.
- 1983. The form and dynamics of Langmuir circulations. *Ann. Rev. Fluid Mech.*, 15, 391–427.
- Leibovich, S., S. K. Lele and I. M. Moroz. 1989. Nonlinear dynamics in Langmuir circulations and in thermosolutal convection. *J. Fluid Mech.*, 198, 471–511.
- Leibovich, S. and S. Paolucci. 1980. The Langmuir circulation instability as a mixing mechanism in the upper ocean. *J. Phys. Oceanogr.*, 10, 186–207.
- 1981. The instability of the ocean to Langmuir circulations. *J. Fluid Mech.*, 102, 141–167.
- Melander, M. V., N. J. Zabusky and J. C. McWilliams. 1988. Symmetric vortex merger in two dimensions: causes and conditions. *J. Fluid Mech.*, 195, 303–340.
- Pollard, R. T. 1977. Observations and theories of Langmuir circulations and their role in near surface mixing, *in A Voyage of Discovery: George Deacon 70th Anniversary Volume*, M. Angle, ed., Pergamon Press, New York, 235–251.
- Richman, J. and C. Garrett. 1977. The transfer of energy and momentum by the wind to the surface mixed layer. *J. Phys. Oceanogr.*, 7, 876–881.
- Smith, J. 1983. On surface gravity waves crossing weak current jets. *J. Fluid Mech.*, 134, 277–299.
- Smith, J., R. Pinkel and R. A. Weller. 1987. Velocity structure in the mixed layer during MILDEX. *J. Phys. Oceanogr.*, 17, 425–439.
- Smith, S. D. 1988. Coefficients for sea surface wind stress, heat flux, and wind profiles as a function of wind speed and temperature. *J. Geophys. Res.*, 93, 15,467–15,472.
- Thorpe, S. A. 1992a. Bubble clouds and the dynamics of the upper ocean. *Quar. J. Roy. Meteor. Soc.*, 118, 1–22.
- 1992b. The breakup of Langmuir circulation and the instability of an array of vortices. *J. Phys. Oceanogr.*, 22, 350–360.
- Weller, R. A. and J. F. Price. 1988. Langmuir circulation within the oceanic mixed layer. *Deep-Sea Res.*, 35, 711–747.
- Zedel, L. and D. Farmer. 1991. Organized structures in subsurface bubble clouds: Langmuir circulation in the open ocean. *J. Geophys. Res.*, 96, 8889–8900.